Available online at www.sciencedirect.com
SCIENCE DIRECT
Planetary and Space Science 53 (2005) 659–670
Planetary and Space Science
www.elsevier.com/locate/pss

Response of the intermediate complexity Mars Climate Simulator to different obliquity angles

J. Segschneider[a,*], B. Grieger[a], H.U. Keller[a], F. Lunkeit[b], E. Kirk[b], K. Fraedrich[b], A. Rodin[c], R. Greve[d,1]

[a]*Max-Planck-Institut für Aeronomie, Max-Planck-Str. 2, D-37191 Katlenburg-Lindau, Germany*
[b]*Meteorologisches Institut, Universität Hamburg, Bundestr. 55, D-20146 Hamburg, Germany*
[c]*Space Research Institute, Ul. Profsoyuznaya 84/32, Moscow, Russia*
[d]*Fachbereich Mechanik, Technische Universität Darmstadt, Hochschulstrasse 1, D-64289 Darmstadt, Germany*

Received 31 July 2003; received in revised form 30 June 2004; accepted 13 October 2004
Available online 1 February 2005

Abstract

A climate model of intermediate complexity, named the Mars Climate Simulator, has been developed based on the Portable University Model of the Atmosphere (PUMA). The main goal of this new development is to simulate the climate variations on Mars resulting from the changes in orbital parameters and their impact on the layered polar terrains (also known as permanent polar ice caps). As a first step towards transient simulations over several obliquity cycles, the model is applied to simulate the dynamical and thermodynamical response of the Martian climate system to different but fixed obliquity angles. The model is forced by the annual and daily cycle of solar insolation. Experiments have been performed for obliquities of $\phi = 15^\circ$ (minimum), $\phi = 25.2^\circ$ (present), and $\phi = 35^\circ$ (maximum). The resulting changes in solar insolation mainly in the polar regions impact strongly on the cross-equatorial circulation which is driven by the meridional temperature gradient and steered by the Martian topography. At high obliquity, the cross-equatorial near surface flow from the winter to the summer hemisphere is strongly enhanced compared to low obliquity periods. The summer ground temperature ranges from 200 K ($\phi = 15^\circ$) to 250 K ($\phi = 35^\circ$) at 80°N in northern summer, and from 220 K ($\phi = 15^\circ$) to 270 K ($\phi = 35^\circ$) at 80°S in southern summer. In the atmosphere at 1 km above ground, the respective range is 195–225 K in northern summer, and 210–250 K in southern summer.

Keywords: Mars; Mars climate; Mars atmosphere; Climate modelling; Atmospheric dynamics

1. Introduction

Mars not only is our direct neighbour, but also the most earthlike planet in the solar system. The atmospheric dynamics and the climate on Mars and Earth, however, are different in many aspects. Liquid water in the form of oceans is completely absent from Mars, resulting in low thermal inertia and thus rapid temperature changes in response to radiation changes. As a consequence so-called thermal tides, i.e., pressure and temperature variations in response to the diurnal cycle of insolation, are a major source of variability on daily time scales. The large eccentricity of the orbit around the sun results in an asymmetric seasonal cycle of insolation. In southern summer insolation is 30% higher than in northern summer. The atmosphere consists of 95% CO_2 that condenses in the winter polar region and sublimes in the summer polar region with a turnover of 25% of the atmospheric mass. On the interannual time scale, dust storms are thought to be the major source of

*Corresponding author. Max-Planck-Institut für Meteorologie, Bundesstr. 53, D-20146 Hamburg, Germany. Fax: +49 40 41173 240.
E-mail address: segschneider@dkrz.de (J. Segschneider).
[1]Institute of Low Temperature Science, Hokkaido University, Kita-19, Nishi-8, Kita-ku, Sapporo 060-0819, Japan.

0032-0633/$ - see front matter © 2004 Elsevier Ltd. All rights reserved.
doi:10.1016/j.pss.2004.10.003

variability. Dust in the Martian atmosphere has to some extent the same effect as aerosols on Earth, namely to absorb short wave radiation and to shield off the surface, resulting in a temperature increase at high altitudes and a cooling near the surface. Due to normally low dust concentrations, the atmosphere is almost transparent and thus heating from the ground normally drives the atmospheric circulation. This heating from below varies spatially due to the large surface elevation differences on Mars. Only during major dust storms a complex interplay of the short wave and thermal IR fluxes scattered in the atmosphere affects the circulation.

On time scales of 10^5–10^6 years, Mars experiences large periodic changes of the orbital elements obliquity (ϕ), eccentricity (ε) and longitude of perihelion with respect to the ascending node (λ_p). These changes impact on the Martian climate. The obliquity determines the latitudinal distribution of solar insolation. The eccentricity determines the magnitude of the asymmetry of insolation with season, and the longitude of perihelion relative to the ascending node determines the timing of the asymmetry of solar insolation with season. Currently, Mars is closest to the sun in southern summer ($\lambda_p = 250.87$), when global mean solar insolation is 30% higher than in northern summer.

On Earth, so-called Milankovitch cycles of much weaker orbital changes with periods of 20, 40 and 100 kyr are considered driving forces for climate variations like the glacial/interglacial cycles (Milankovitch, 1930). It can, therefore, be expected that the main Martian $\pm 10^\circ$ obliquity cycles with periods of 125 kyr and 1.3 Myr have a significant impact on climate due to large insolation changes in the polar regions (Kieffer and Zent, 1992). A recalculation of ϕ, ε, and λ_p for the last 10 million years has been published recently by Laskar et al. (2002).

In this study we aim at simulating the impact of different obliquity angles on surface and near surface temperature and circulation with a numerical model. Our goal is not to give a comprehensive description of the thermodynamic and dynamic behaviour of the martian atmosphere, which has been done elsewhere. We are more interested in the near surface behaviour, as our final goal is to understand the mechanisms that cause the layering of the ice caps. Since most of the water vapour must be transported at lower levels, were it is more abundant, the upper levels are not the main subject of our study, even though the strongest flow is occurring at larger height. In a companion paper (Greve et al., 2004), the impact of orbital changes on the north polar ice cap is investigated.

After initial studies in the late 1960s (Leovy and Mintz, 1969), numerical modelling of the present Martian atmosphere intensified mainly triggered by the successful Viking missions in the late 1970s. The more recent successful orbiter missions, Mars Global Surveyor (MGS, launched 1996), and Mars Odyssey (launched 2001) and now Mars Express (2003) have brought a new wealth of observational data that will boost the numerical model development. Established modelling groups work at LMD, Paris and AOPP, Oxford on the European GCM (Read et al., 1997; Forget et al., 1999), at the NASA/Ames research center in Moffett Field on the NASA AMES GCM (Haberle et al., 1993), at Princeton, New Jersey and Caltech, Pasadena on the 'SKYHI' model (Wilson and Hamilton, 1996), and at distributed institutes in Japan (Takahashi et al., 2003). The models, all derivatives of Earth General Circulation Models (GCMs), solve the equations of fluid dynamics and include the processes of radiative transfer, cloud formation, regolith-atmosphere water exchange, and advective transport of dust and trace gases. They take into account the topography of the Martian surface and include the altitude region between 0 and about 120 km. These state-of-the-art models reproduce the observed temperature structure, pressure variations and water cycle reasonably well.

Recent studies investigated the role of the topographic asymmetry (northern lowlands, southern highlands) on the Hadley circulation (Richardson and Wilson, 2002; Takahashi et al., 2003), the role of dust with an active dust module in the AOPP/LMD model (Newman et al., 2002), and the thermal circulation over a Martian volcano with a mesoscale model (Rafkin et al., 2002). Most similar to what is attempted here, a paleo study investigating the impact of orbital parameters mainly on dust lifting potential has been performed with the AMES model (Haberle et al., 2003).

All these models, however, have in common that they are designed to simulate the present atmosphere as best as possible. Consequently, they are computationally expensive. Cheap, simple one-dimensional models have been used to study specific processes that do not require full solution of the dynamic equations. Examples are the radiative transfer model by Gierasch and Goody (1968), regolith-atmosphere water exchange by Jakosky (1985) and water ice cloud formation by Michelangeli et al. (1993). The Mars Climate Simulator is designed to close the gap between these simple models and the fully complex GCMs to investigate mainly the paleo climate of Mars. Models of its type, so-called EMICs (Earth Models of Intermediate Complexity), have successfully been used to simulate terrestrial climate transitions (Ganopolski et al., 1998; Claussen et al., 2002).

2. The model basis for the Mars Climate Simulator

The development of the Mars Climate Simulator is based on the PUMA atmospheric GCM (Portable University Model of the Atmosphere, Fraedrich et al.,

1998) with added components for the land surface, radiation, precipitation, clouds, and, if desired, an active ocean (documentation in preparation). PUMA is based on the Reading multi-level spectral model SGCM (Simple Global Circulation Model) described in Hoskins and Simmons (1975). Originally developed as a numerical prediction model, it was changed to perform as a general circulation model. PUMA was developed at the University of Hamburg with the following aims in mind: compatibility with the ECHAM (European Centre HAMburg) GCM, portability between different computing platforms, and training of junior scientists.

The code is rewritten in portable Fortran-90 without using any external libraries. It has been tested on platforms ranging from Pentium-PCs to vector/parallel super computers. The truncation scheme is changed from jagged triangular truncation to standard triangular truncation that is compatible to other T-models like ECHAM. The model output is such that it can be processed with the ECHAM afterburner, which allows the use of the ECHAM diagnostic software packages for interpretation of the PUMA output.

The initial PUMA code was basically the dynamical core of a GCM forced by Newtonian cooling and Rayleigh friction. It formed the basis for various applications: the code has been utilized to build and test new numerical algorithms like semi-Lagrangian techniques, to perform idealized experiments to analyze nonlinear processes arising from internal dynamics of the atmosphere, and for data assimilation purposes to interpret results from GCM simulations or observations.

The model solves the primitive equations formulated in terms of the vertical component of absolute vorticity ζ and the horizontal divergence D to compute the three dimensional temperature distribution, and velocity fields from spectral vorticity and divergence. Vertical diffusion representing the non resolved turbulent exchange is applied to the horizontal wind components, the potential temperature and to specific humidity if the latter is included in the model computations. Horizontal diffusion is done in spectral space based on the ideas of Laurson and Eliasen (1989). The bottom friction is computed using local Richardson Number dependent drag coefficients.

Based on the dynamical kernel, the model has been extended by modules that compute specific humidity, cloud cover and precipitation, radiative cooling and heating in the short and long wave range, soil temperature and wetness, snow temperature and depth, the albedo and the surface roughness. Glaciers can be introduced using a maskfile. Glaciers have fixed ice albedo and soil humidity. The extended version of PUMA is referred to as Planet Simulator.

The radiation scheme allows for two wavelength bands in the solar range, while the thermal radiation code does not distinguish between different wavelengths. The solar radiation code computes up and downward fluxes and corresponding heating rates from the incoming radiation at the upper boundary of the atmosphere. The code computes transmissivity and reflectance from relative humidity, fixed CO_2 concentration, (water) cloud cover, and surface albedo. Surface albedo for land points is mainly a function of temperature and vegetation, with special values for ice covered areas.

3. Adaptation to Mars

All planet dependent physical parameters, like the radius, rotation rate, gas constant, lapse rate, etc. (see Table 2, Appendix A) have been replaced by Martian values. The additional dependence of the albedo on vegetation cover and temperature for values between 273 and 283 K was removed. A new subroutine has been introduced to initialize the model with more balanced temperature fields that take into account the large range of Martian topography by adjusting the bottom temperature using the average lapse rate ($2.5\,\mathrm{K\,km^{-1}}$). This proved necessary to keep the model numerically stable.

The model domain is confined to the Martian troposphere. The number of σ-levels (p/p_0, where p_0 is the local surface pressure) has been doubled to 10 (unevenly distributed, listed in Table 1) to better resolve the steeper Martian topography. The horizontal resolution is T21 ($\approx 5.6^\circ$). The time step has been reduced from 60 to 15 min dictated by the pronounced topography and the smaller grid boxes on Mars. The Martian year of the MCS consists of 12 months of 56 days length. A day has 24 h of 61.5 min length, a minute is still 60 s long.

The Mars topography derived from the Mars Orbiting Laser Altimeter (MOLA, e.g. Smith et al., 1999) $1^\circ \times 1^\circ$ measurements has been introduced into the model. The topography is not artificially smoothed, but interpolated to the $5.6^\circ \times 5.6^\circ$ T21 model grid, resulting in averaging out some smaller scale features but still

Table 1
Model level, $\sigma(p/p_0)$, and height above topography in km for the Martian set-up of the model

Model level	σ	Height (km)
1	0.038	35.2
2	0.119	23.0
3	0.211	16.8
4	0.317	12.4
5	0.437	8.9
6	0.567	6.1
7	0.699	3.8
8	0.823	2.1
9	0.924	0.9
10	0.983	0.2

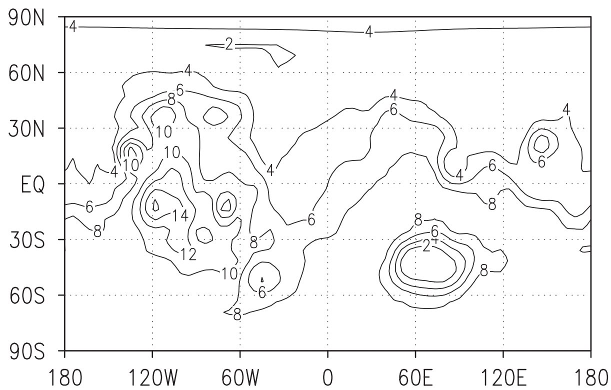

Fig. 1. MOLA topography on the model grid in km, normalized to positive values.

retaining the major volcanos and impact craters as separate features. The topographic range after interpolation is still more than 14 km (Fig. 1). Note that this is considerably more than for the terrestrial set-up and that Mars has a smaller radius, thus limiting the range to which the model's time step can be extended.

The model is driven by the seasonal and daily cycle of solar insolation. The forcing takes into account the eccentricity of the orbit, the moving longitude of perihelion, and the obliquity of the Martian rotation axis following Berger (1978). Heating rates for the Martian surface are computed from the local solar insolation taking into account the Martian albedo, the specific heat of the surface material, and the thermal diffusivity (see Appendix A).

The radiative transfer module has been adapted such that the short wave part assumes an almost transparent atmosphere (a so-called low dust scenario). The long wave transmissivities have been adjusted according to the bulk transmissivity for Mars from energy balance considerations. For a solar constant of $587\,\mathrm{W\,m^{-2}}$, a planetary albedo of 0.24, and an equilibrium temperature of 214 K, the bulk transmissivity is 0.914, that is, only 8.6% of the long wave radiation are available for heating the atmosphere. A further pressure scaling is applied to allow for the variable topography and hence variable pathway of the radiation. The local profile of transmissivity is then computed as

$$Tr(\varphi, \lambda, \sigma) = 1 - (\alpha \cdot \mathrm{e}^{\sigma(z) \cdot p_{\mathrm{sfc}(\varphi,\lambda)}/p_{\mathrm{mean}}}), \tag{1}$$

where α is a tunable scaling factor, p_{mean} is the global mean surface pressure of 627 Pa, $p_{\mathrm{sfc}(\varphi,\lambda)}$ is the local surface pressure, φ is the geographical latitude and λ the geographical longitude. The scaling factor α is initially chosen so that the average absorption over all locations and layers for $\alpha = 0.065$ is about 8.5%. The scaling factor was then further used to tune the long wave radiation scheme to allow for the effects of dust and water vapour and ice clouds not included in the model. The results presented here were computed with $\alpha = 0.12$. Smaller values resulted in unrealistic temperature intermediate maxima at greater height in the winter hemisphere.

The model has no active CO_2 and thus is not suitable for studying the seasonal pressure cycle. It is thus possible for the atmospheric temperature to drop below the condensation point of CO_2. While it is foreseen to incorporate active CO_2 in the future for comparison of model data with future mission data, it has been shown that the seasonal pressure cycle is not crucial for paleo studies (Haberle et al., 2003). To simulate the effect of the seasonal CO_2 frost caps, a simple parameterization is introduced that sets the albedo to 0.6 for surface temperatures of less than 148 K. While this is a very simple approach, it results in a delay of the spring warming similar to that simulated by Haberle et al. (2003).

4. Results

Results are shown for three model experiments. In these experiments, the model is forced by the seasonal cycle of solar insolation for different obliquity values. The obliquity ϕ varies from 15°, the minimum value, to 25.2°, the present value, and 35°, the maximum value during the last 5 million years (Laskar et al., 2002). The eccentricity ε is kept constant in all experiments at the present value of 0.093 and the longitude of perihelion λ_{p} at 250.87°.

Due to the inherited post-processing procedures and the requirement to keep these for future comparisons with Earth, the model output is presented relative to time using equal length calendar months. Since the eccentricity is much larger for Mars than for Earth, the position on the orbit (L_{s} for solar longitude) does not change linearly with time. The relation is given in Fig. 2 which shows that the deviation can be up to 10° (1 July corresponding to 79.13° rather than 90°), which corresponds to 30 July or day 360. This has to be kept in mind when comparing results with L_{s}-based output.

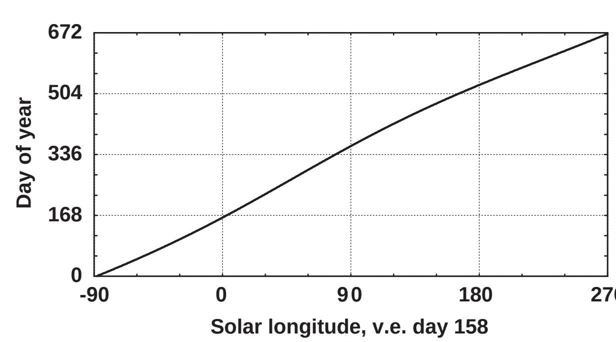

Fig. 2. Solar longitude L_{s} vs. day of the year for $\varepsilon = 0.093$, vernal equinox (v.e.) day 158, and longitude of perihelion = 250.87° computed following Berger (1978).

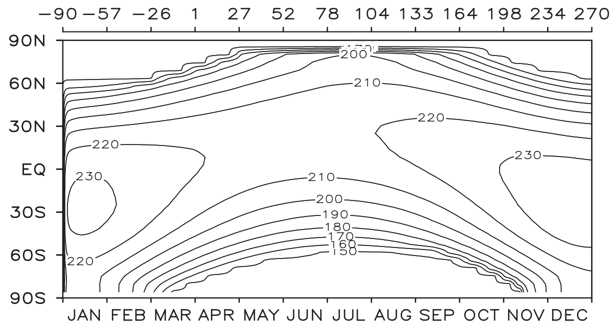

Fig. 3. Seasonal cycle of ground temperature (K) for an obliquity angle of 15°. Shown are daily and zonally averaged means. The contour interval is 10 K. The upper *x*-axis gives solar longitude (L_s) in (deg), the lower *x*-axis label are the month of the year. The step-like features of the 150 K contour line are the result of the coarse model resolution and the albedo parameterization.

Also, the computations start on 1 January at $L_s = -90$, not $L_s = 0$. Solar longitude is also indicated for the beginning of each calendar month at the top of Figs. 3 and 4.

For comparison with Fig. 6 in Haberle et al. (1993) we include Fig. 3. The figure shows the seasonal cycle of zonal mean ground temperature for an obliquity of 15° (the only matching angle) and agrees fairly well with the respective temperatures from the AMES model (second panel from top in their figure).

4.1. Thermal response

As a result of the change in obliquity, the latitudinal distribution of radiation changes, with largest effects in the polar regions. This is demonstrated by Fig. 4a. The figure shows the annual cycle of net incoming radiation, i.e., solar insolation minus reflected short wave radiation at 80°N and 80°S for one Martian year and the three obliquity angles. Different obliquity results in differences of the maximum net incoming radiation. It varies between 120 W m^{-2} for $\phi = 15°$ and 300 W m^{-2} for $\phi = 35°$ at 80°S, and between 90 W m^{-2} and 210 W m^{-2} at 80°N. The step-like features in April and October are the result of the albedo parameterization of the seasonal CO_2 ice cover. For temperatures of less than 148 K the albedo is set to 0.6, for higher temperatures to 0.2. Remember that net incoming radiation is shown. When insolation slowly increases in spring, it takes some time for the ground to heat up and to 'melt' the CO_2 ice, so a large fraction of the radiation is reflected back to space. The reflected fraction then becomes suddenly smaller, when the temperature exceeds 148 K.

The variations in ϕ and thus radiative energy input have considerable impact on the temperature of the regolith and atmosphere (Figs. 4b and c). The maximum surface temperatures vary from 220 K for $\phi = 15°$ to 265 K for $\phi = 35°$ at 80°S, and from 195 K for $\phi = 15°$ to 250 K for $\phi = 35°$ at 80°N. Again, the asymmetry

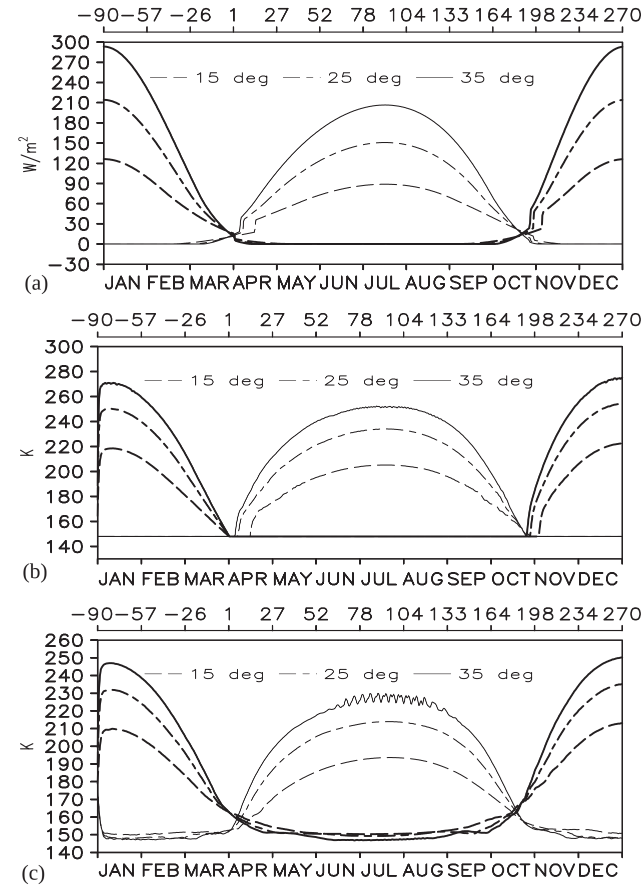

Fig. 4. (a) Annual cycle of net incoming radiation (see text for definition), (b) surface temperature, and (c) atmospheric temperature at 1 km height. Shown are curves for 80°N (thin) and 80°S (bold) for obliquity angles of 15° (dashed), 25.2° (dot–dashed) and 35° (solid). The upper *x*-axis gives solar longitude (L_s) in (deg), the lower *x*-axis label are the month of the year.

between the hemispheres is caused by the eccentricity of the orbit. While the absolute temperatures differ, the range of the variations is the same. With respect to the final goal, the investigation of the driving forces of the layered polar terrains, it is worthwhile to note that the differences of 45 K are likely to result in changes of the amount of water vapour evaporated from any subsurface reservoirs. Changing atmospheric water vapour content could be a mechanism to explain the layering of the polar caps. Unfortunately, we do not yet have a good model basis to investigate this. Fig. 4b also shows that the response to changed ϕ is not linear (25° and 35° being more similar than 15° and 25°). Also the seasonal behaviour is asymmetric: there is an offset in the timing of the onset of spring temperature rise caused by the time required to 'melt' the CO_2 frost: for lower obliquities, it takes longer to raise the temperature to more than 148 K, at which point the albedo switches from 0.6 to 0.2. The autumnal cooling reaches the condensation temperature of 148 K at the same time for all three obliquities.

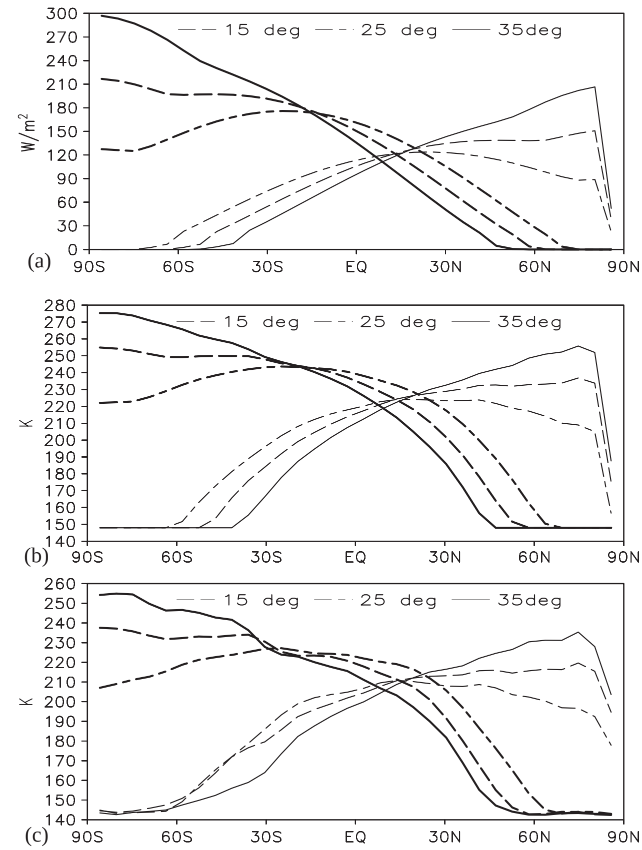

Fig. 5. Zonal mean of (a) net incoming radiation, (b) surface temperature, and (c) atmospheric temperature at 1 km height in southern summer (L_s270, bold) and northern summer (L_s90, thin) for different obliquity angles: 15° (dashed), 25.2° (dot–dashed) and 35° (solid).

The seasonal cycle of the atmospheric temperature is very similar to that of the ground temperature. This can be expected since the Martian atmosphere is mainly heated from the ground. Advection and horizontal diffusion, however, act against the temperature gradients that result from radiation, so deviations from the purely local response of the surface regolith are possible. The maximum temperatures at 1 km height are somewhat lower than for the regolith. An interesting feature is the occurrence of short time scale variability in northern summer for $\phi = 35°$ at 80°N. Obviously, the temperature gradient at the outer boundary of the permanent ice cap exceeds some critical value. We will come back to this later at the end of Section 4.2, Fig. 9.

In the next paragraphs, the latitudinal distribution of properties is investigated. The impact of obliquity on net incoming radiation and the latitudinal temperature distribution is presented in Fig. 5. Fig. 5a shows that for high obliquity the radiation maximum is at the pole for southern summer and close to the pole for northern summer. The impact of the permanent ice cap (simulated as increased albedo) is clearly visible as a sharp decrease in net radiation towards the pole north of 80°N. For low obliquity the maximum is closer to the equator. Fig. 5b shows zonal averages of the ground temperature. For smaller obliquity, the curves become flatter, with the maximum shifting towards the equator and the 148 K point shifting poleward by some 20°. All curves cross at 15° latitude of the summer hemisphere where the $\phi = 15°$ curves show close to maximum values. The distribution directly reflects the heating from solar radiation. As in Fig. 5a, the north polar cap shows up clearly with summer surface temperatures not exceeding 180 K for $\phi = 35°$ as a result of the high albedo of the permanent water ice.

The latitudinal distribution of the atmospheric temperatures is shown in Fig. 5c for a height of 1 km above the ground. To first order the structure reflects the heating from the ground but summer maxima of 210 K ($\phi = 15°$, northern summer) to 255 K ($\phi = 35°$, southern summer) are some 20 K colder than the ground below. In winter the atmospheric temperature is quite close to the surface value of 148 K. The pole-to-pole temperature gradient (excluding the north polar cap) ranges from 40 K ($\phi = 15°$, northern summer) to 100 K ($\phi = 35°$, southern summer). The impact of obliquity on temperature is largest at the south pole, where temperatures range from 210 K ($\phi = 15°$) to 255 K ($\phi = 35°$). Close to the north pole the respective values range from 195 to 235 K, but are much lower over the permanent ice cap. The temperature differences on the winter hemisphere are small polewards of 60°N/S since the incoming radiation is zero for all obliquities.

The atmospheric temperatures are sensitive to the obliquity in summer, but winter temperatures remain largely unaffected. The variations in the atmosphere are smaller than for the surface regolith. Also the effect of higher insolation in southern summer is partly compensated by the higher surface elevation on the southern hemisphere.

4.2. Dynamic response

In this section the dynamic response of the model to the different obliquity angles is described. Results are first shown as global maps of atmospheric temperature at a height of 1 km above ground. Vertical sections will be shown later. Figs. 6a and d show the northern summer conditions for $\phi = 15°$. The temperature distribution (Fig. 6a) is the combined result of the net solar insolation, the topography of Mars, and the dynamic response of the model, i.e., advective heat transport. The temperatures range from less than 150 K in the south polar (winter) region to 220 K in the low-elevated areas at around 30°N. The deviations from the zonal mean are mainly the result of topography (higher areas being colder).

The circulation (Fig. 6d) shows some small scale features in the vicinity of the strong topographic

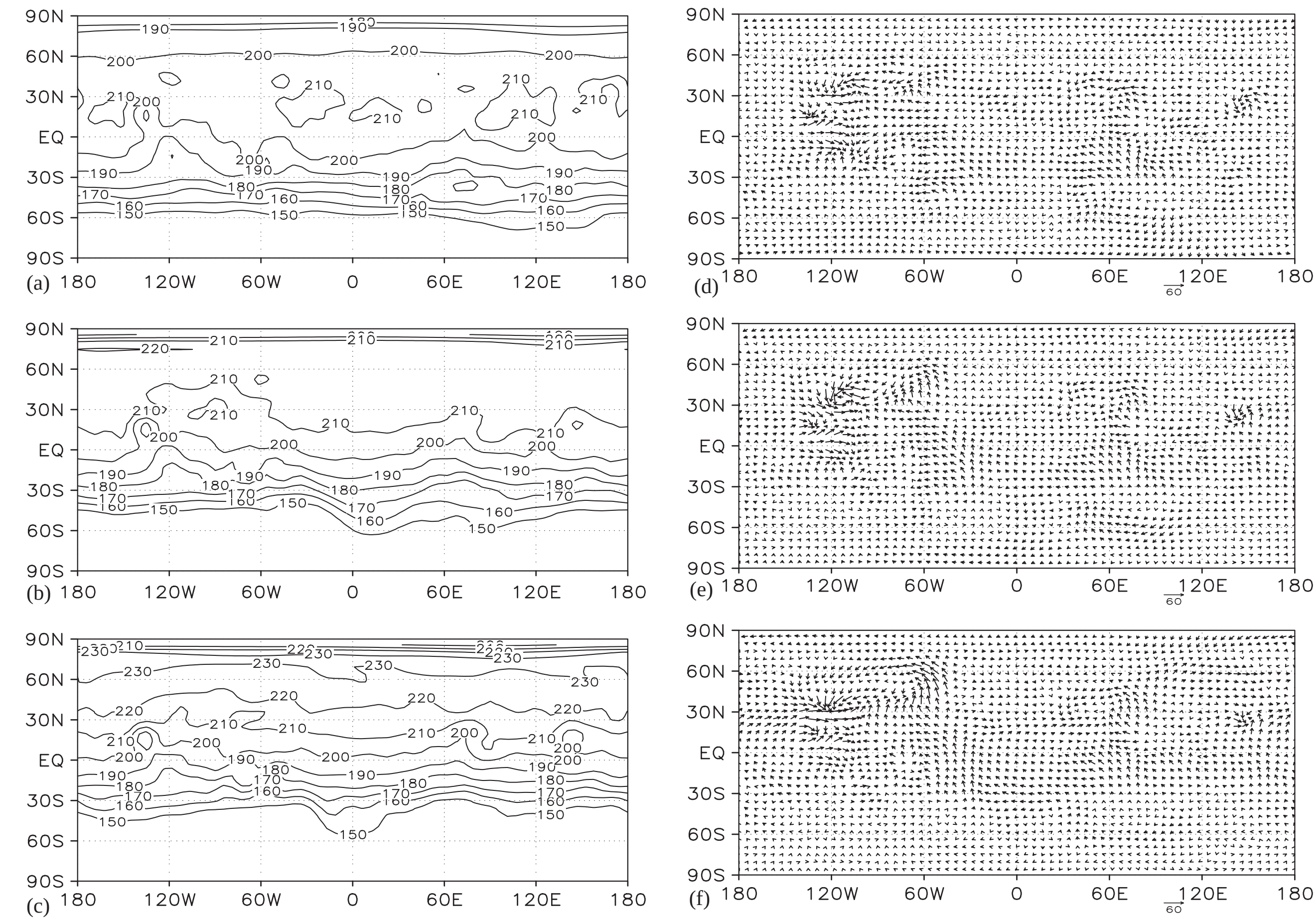

Fig. 6. Atmospheric temperature in K (a–c) and wind field in m s^{-1} (d–f) at a height of 1 km for northern summer (L_s90) for an obliquity of (a,d) 15°, (b,e) 25.2°, and (c,f) 35°. The scale arrow corresponds to 60 m s^{-1}.

gradients embedded in the large scale circulation in response to the latitudinal temperature gradients. The wind speeds are fairly high compared to terrestrial standards, with maxima at around 60 m s^{-1} north of the Hellas Basin and in the vicinity of the Tharsis region. The small scale circulation is relatively unaffected by the obliquity as it is mainly determined by the topography. The large scale features like the areas of strong flow around 60°E and west of 60°W exhibit a shift from more zonal flow ($\phi = 15°, \phi = 25°$, Figs. 6d and e) to more meridional flow ($\phi = 35°$, Fig. 6f). In particular for the latter obliquity, a strong south to north cross-equatorial flow is present while for lower obliquities the cross-equatorial flow is only small. These western boundary currents along the topographic slopes are investigated in fair detail for the present day obliquity in Joshi et al. (1995).

The respective maps of temperature and circulation for southern summer (L_s270) are shown in Fig. 7. For $\phi = 15°$ (Fig. 7a) maximum temperatures are more than 220 K south of the equator and in the Hellas and Argyre basin. Note that, as opposed to northern summer, already for $\phi = 15°$ the circulation has a strong cross-equatorial component (Fig. 7d). Southern summer temperatures are higher than for northern summer on the respective summer hemisphere because Mars is closer to the Sun. As winter temperatures are similar on both hemispheres, this results in a stronger inter-hemispheric temperature gradient and hence intensified Hadley circulation. As for northern summer, the cross-equatorial flow intensifies with increasing obliquity (Figs. 7e and f), turning eastward at around 30°S where the meridional temperature gradients become weaker (see also Fig. 5).

In summary, the horizontal temperature distribution is mainly determined by solar insolation and to second order by the topography. The summer season intensifies with increasing obliquity, as can be expected. The dynamic response, however, reveals some interesting patterns. This is demonstrated by Fig. 8 which shows the difference maps of Figs. 6a,c and d,f and 7a,c and d,f. Most of the topographically induced small scale features show little sensitivity to obliquity and thus do not show up on the difference map. The large scale differences are strongest in a latitude band between 60°N and 60°S, where also the largest absolute values of wind speed are simulated. The strong temperature differences at the summer pole, however, are not reflected in large

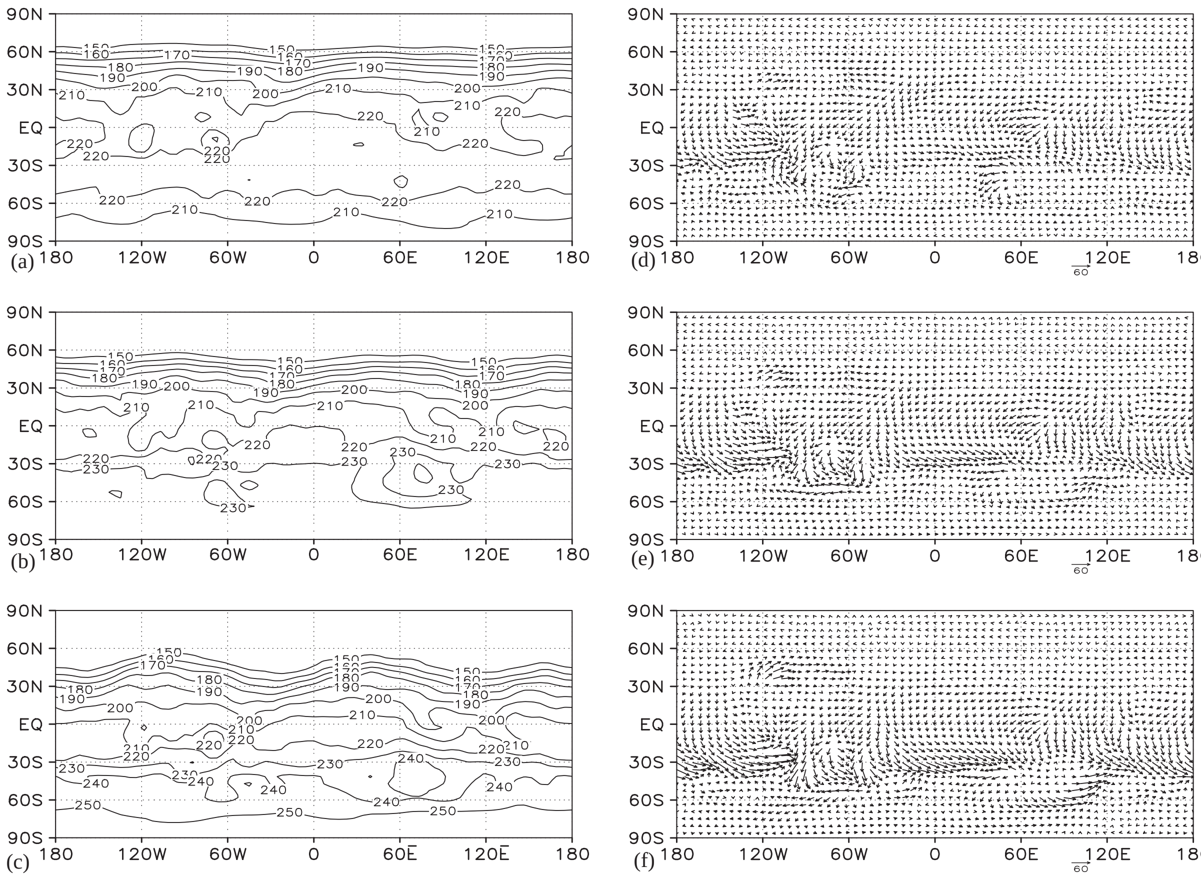

Fig. 7. Atmospheric temperature in K (a–c) and wind field in m s^{-1} (d–f) at a height of 1 km for southern summer (L_s270) for an obliquity of (a,d) 15°, (b,e) 25.2°, and (c,f) 35°. The scale arrow corresponds to 60 m s^{-1}.

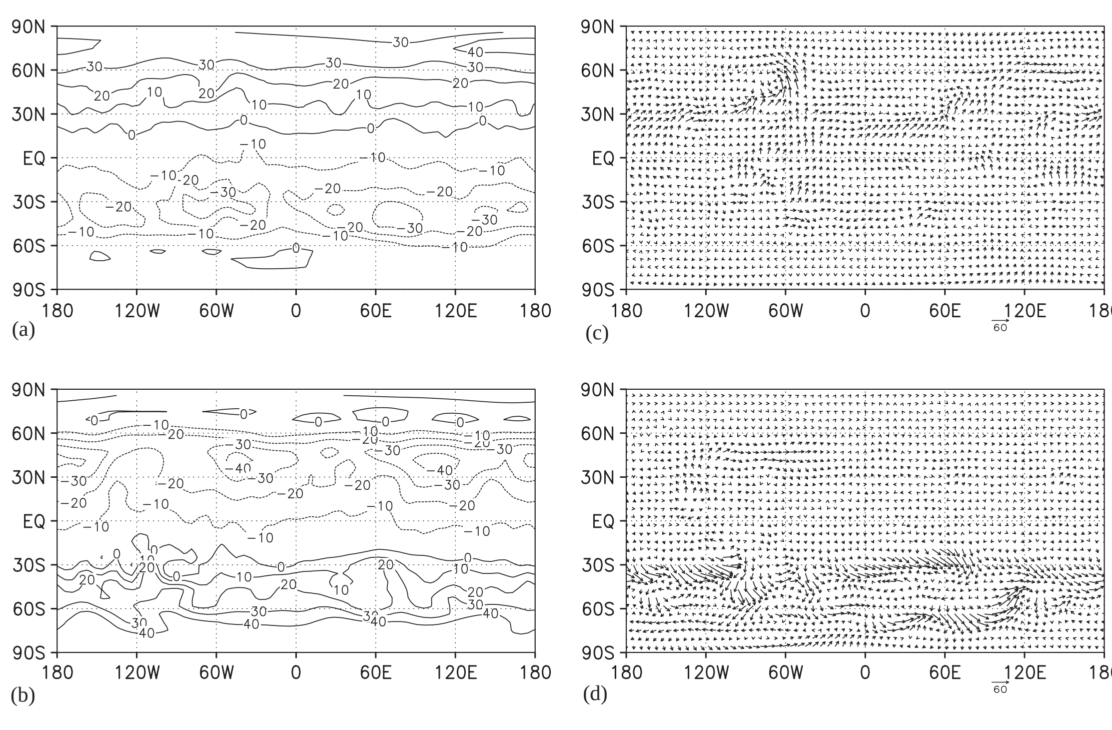

Fig. 8. Difference of atmospheric temperature in K (a,b) and wind field in m s^{-1} (c,d) at 1 km height for $\phi = 35°$ minus $\phi = 15°$ for (a,c) northern summer (L_s90) and (b,d) southern summer (L_s270). The scale arrow corresponds to 60 m s^{-1}.

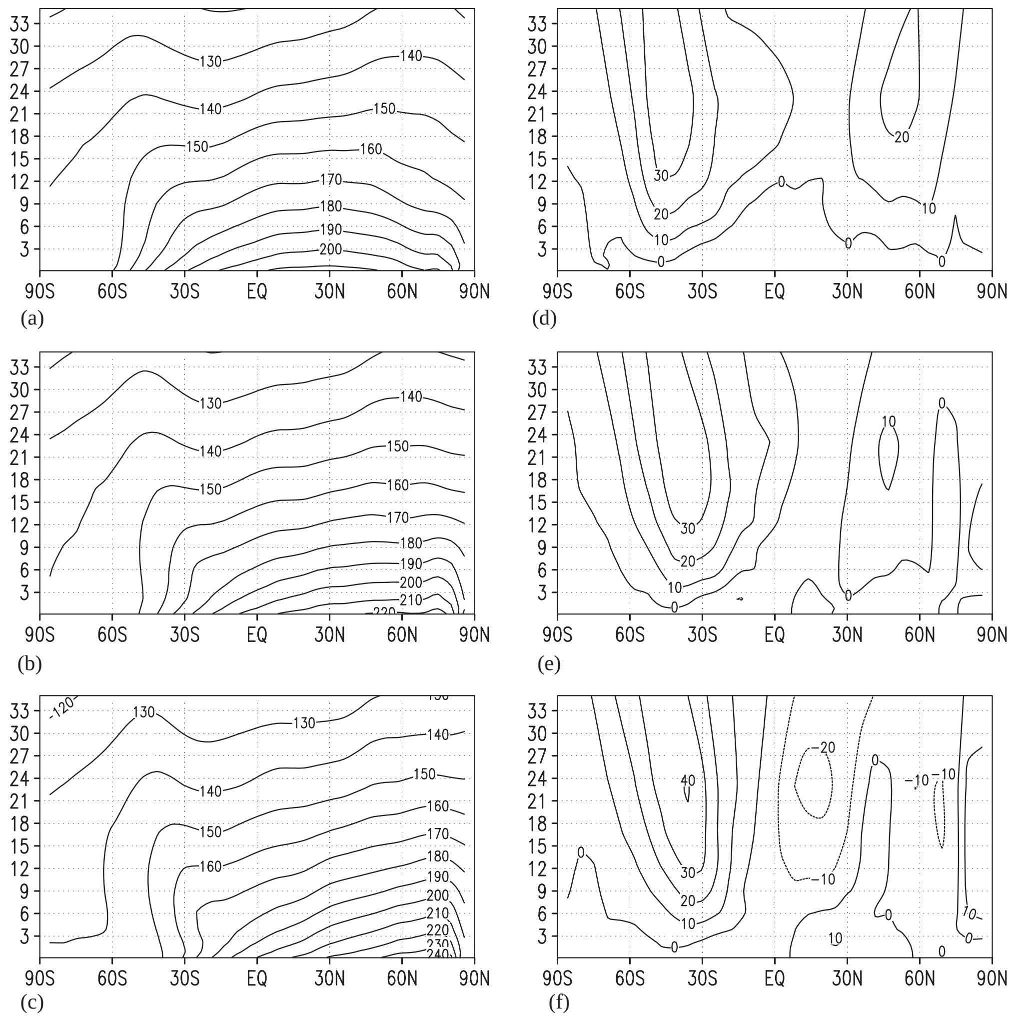

Fig. 9. Vertical sections of zonal means of atmospheric temperature in K (a–c, contour interval 10 K) and zonal velocity in $\mathrm{m\,s^{-1}}$ (d–f, contour interval $10\,\mathrm{m\,s^{-1}}$, negative, i.e. westward values are stippled) for northern summer (L_s90) for an obliquity of (a,d) 15°, (b,e) 25.2°, and (c,f) 35°. The height is given in km.

differences of the velocity fields, since the meridional gradients remain small for all obliquities while the absolute values change.

For southern summer, the area of strong sensitivity of atmospheric circulation to obliquity is mainly focused at a latitude band of 30°S to 60°S, and also around 30°N to 60°N. The southern zone reflects a poleward shift (in addition to the intensification) of the wind field (see also Figs. 7d–f) while the northern part reflects decreasing velocities in response to increasing obliquity and hence a move of the latitude of strong temperature gradients.

Height-latitude sections of temperature and zonal velocity are shown in Figs. 9 and 10. The most prominent feature in northern summer is an eastward jet with speeds of around $40\,\mathrm{m\,s^{-1}}$, centred at around 40°S and 15 km height (Figs. 9d–f). This jet intensifies with increasing obliquity as a result of the increased temperature gradient in response to the incoming radiation. A weaker jet on the northern hemisphere of about $20\,\mathrm{m\,s^{-1}}$ centred at around 50°N is simulated for $\phi = 15°$ (Fig. 9a). It weakens with increasing obliquity ($\phi = 25°$, Fig. 9b) and even reverses for an obliquity of $\phi = 35°$ (Fig. 9c), thereby moving towards the equator. The behaviour can be directly inferred from the meridional distribution of the temperature (Figs. 9a–c): The southern hemisphere jet is in the region of the largest horizontal temperature gradients. The northern hemisphere jet is driven by the much weaker temperature gradients at around 30° to 60°N. The slope towards the north ($\phi = 15°$) is replaced by almost no horizontal gradients for the present obliquity, while the slope is towards the south for $\phi = 35°$.

Note the appearance of the eastward jet close to the north pole for $\phi = 35°$ ($v_{\max}$ more than $20\,\mathrm{m\,s^{-1}}$) as a result of the presence of the north polar cap with high albedo and hence strong temperature gradients (see also Fig. 5). The result is a strong wave activity (Fig. 11) which causes the high frequency (period about 10 days) variations in temperature apparent in Fig. 4c.

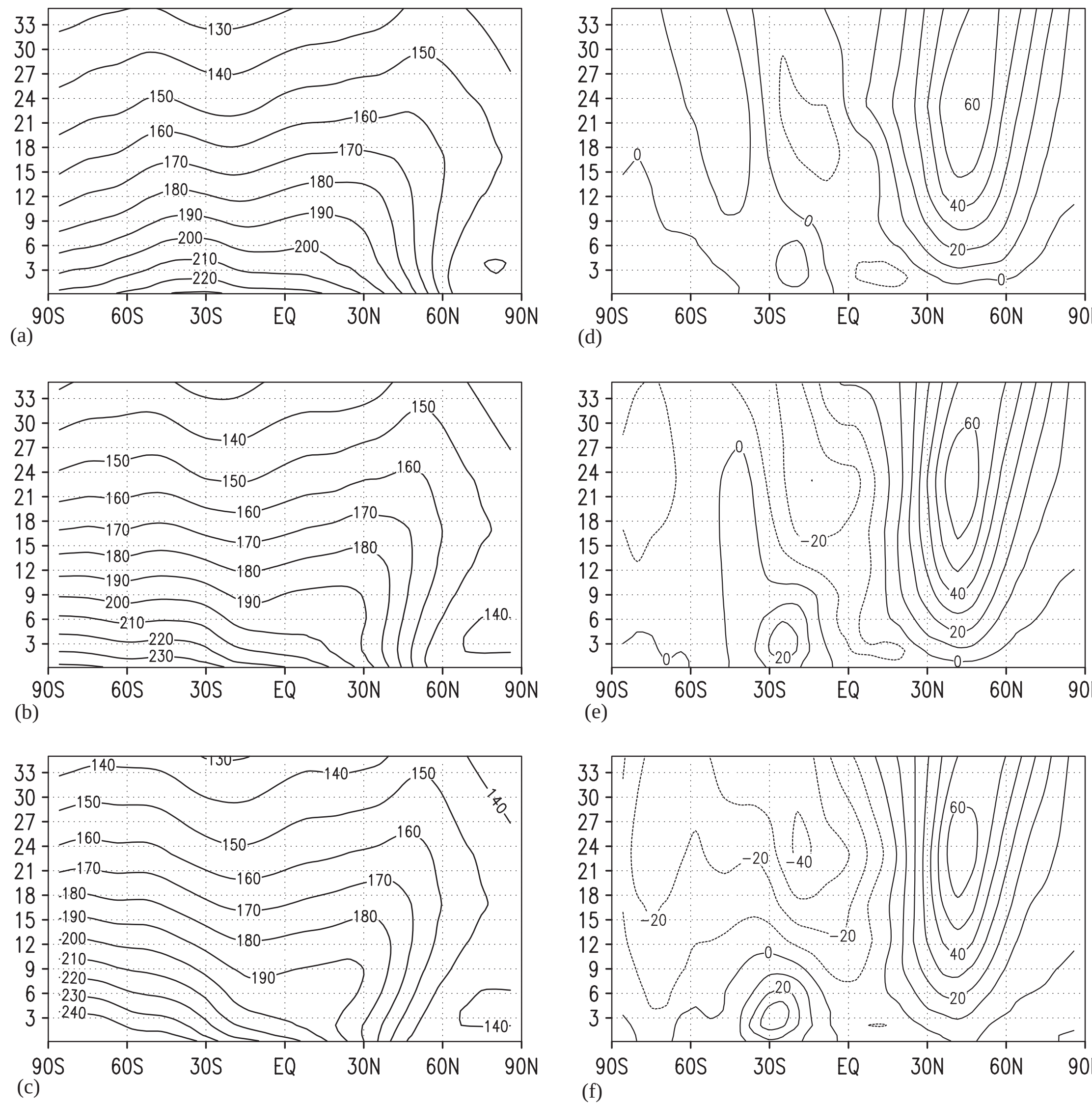

Fig. 10. Vertical sections of zonal means of atmospheric temperature in K (a–c) and zonal velocity in $m\,s^{-1}$ (d–f, contour interval $10\,m\,s^{-1}$) for southern summer (L_s270) for an obliquity of (a,d) 15°, (b,e) 25.2°, and (c,f) 35°. The height is given in km.

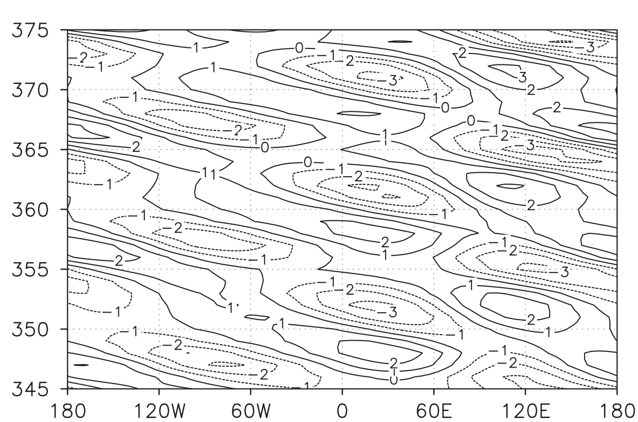

Fig. 11. Longitude–time plot of the deviation of temperature from the time mean for ±15 days centred at L_s90 at a height of 1 km at 80°N.

The vertical temperature distribution above 15 km height shows only little response to obliquity. At heights below 5 km the poleward shift of the temperature maximum in direct response to the amount of incoming radiation dominates the signal.

In southern summer (Fig. 10) the flow direction on the southern hemisphere has reversed compared to northern summer. The winter hemisphere jet (more than 60 compared to $40\,m\,s^{-1}$) is stronger in southern summer. Also there is no counterpart on the summer hemisphere. Instead, flow in the opposite direction is simulated south of the equator. This flow, centred at around 20 km height, shows strong sensitivity to obliquity. The maximum velocities range from $30\,m\,s^{-1}$ ($\phi = 15°$) to more than $60\,m\,s^{-1}$ ($\phi = 35°$). Closer to the surface an eastward jets is prevailing, also intensifying with increasing obliquity.

The zonal wind field is in fair agreement with the results of Hourdin et al. (1993, their Fig. 5). The maximum speed in our model is some 20 m s^{-1} smaller, possibly because the model of Hourdin et al. (1993) extends up to 60 km compared to 40 km for our model. Also the temperatures in the upper layers in our model (based on a lapse rate of 2.5 K km^{-1}) are lower than in the LMD model (with an apparent lapse rate of only 1.5 K km^{-1}, which seems to be more in agreement with MGS and Viking temperature profiles than the widely assumed value of 2.5 km^{-1}) (Kieffer et al., 1992, p. 31).

5. Conclusions

A newly developed intermediate complexity model of the Martian climate system has been used to investigate temperature and circulation in the atmosphere for different obliquity angles. The model has been forced by the seasonal and daily cycle of solar insolation for one Martian year for the minimum ($\phi = 15°$), the present ($\phi = 25.2°$), and the maximum ($\phi = 35°$) obliquity. The thermal response is in direct relation to the radiative forcing. The pole-to-pole temperature difference varies from 40 K for $\phi = 15°$ in northern summer to more than 100 K for $\phi = 35°$ in southern summer. The large scale circulation shows an intensifying Hadley cell and intensifying winter-hemisphere mid-latitude jets for increased obliquity.

Assuming that the layering of the polar terrains is caused by different accumulation rates, the model findings suggest two possible physical mechanisms for variability: More subsurface water ice could be evaporated due to higher temperatures in the summer season, and varying cross-equatorial flow could change the transport rates of water vapour from the summer to the winter hemisphere. This raises the question whether the permanent ice caps grow in winter or in summer. In winter they might be isolated from the atmosphere by the CO_2 frost, and water vapour concentrations should be very small because of the low temperatures. This would imply that the caps grow in summer rather than winter. A next step to investigate this will be the simulation of the Martian water cycle and its interactions with the permanent polar caps, in particular the north polar one.

Acknowledgements

This work was sponsored by the Deutsche Forschungsgemeinschaft under the priority programme 1115, Grant KE226/8-1.

Appendix A

See Table 2.

Table 2
Model parameters adapted to Martian values and their equivalents for Earth

Parameter	Symbol	Earth	Mars	Units
Radius	r	6371	3397	km
Rotation frequency	Ω	7.292	7.0816	$\times 10^{-5}$ s^{-1}
Gravity acceleration	g	9.81	3.74	m s^{-2}
Obliquity of rotation axis	ϕ	23.4 ± 2	25.2 ± 10	deg
Mean distance to Sun		1	1.52	AU
Eccentricity of the orbit	ε	0.017	0.093	
Average lapse rate		6.5	2.5	K km^{-1}
Scale Height	H	7.4	10.8	km
Height of troposphere		12000	40000	m
Gas constant	R	287	188.9	J kg^{-1} K^{-1}
Molecular weight of air		0.0289644	0.0440098	kg mol^{-1}
R/c_p	κ	0.286	0.2273	
Global mean surface temperature	T_{mean}	288	214	K
Global mean albedo	α	0.31	0.24	
Global mean surface pressure	p_{mean}	101325	620	Pa
Constant reference temperature	T_{ref}	250	150	K
Specific heat of surface material	$c_{p,sfc}$	2.4	1	10^6 J m^{-3} K^{-1}
Thermal diffusivity of surface		7.5	1	10^{-7} m^2 s^{-1}

References

Berger, A.L., 1978. Long-term variations of daily insolation and quaternary climatic changes. J. Atmos. Sci. 35, 2362–2367.

Claussen, M., Mysak, L., Weaver, A., Crucifix, M., Fichefet, T., Loutre, M.-F., Weber, S., Alcamo, J., Alexeev, V., Berger, A., Calov, R., Ganopolski, A., Goosse, H., Lohman, G., Lunkeit, F., Mokhov, I., Petoukhov, V., Stone, P., Wang, Z., 2002. Earth system models of intermediate complexity: closing the gap in the spectrum of climate system models. Climate Dyn. 18 (7), 579–586.

Forget, F., Hourdin, F., Fournier, R., Hourdin, C., Talagrand, O., Collins, M., Lewis, S.R., Read, P.L., Huot, J.-P., 1999. Improved general circulation models of the Martian atmosphere from the surface to above 80 km. J. Geophys. Res. 104, 24,155–24,175.

Fraedrich, K., Kirk, E., Lunkeit, F., 1998. PUMA: portable University model of the atmosphere. DKRZ Technical Report 16, DKRZ-Hamburg, available at http://puma.dkrz.de/puma

Ganopolski, A., Rahmsdorf, S., Petoukhv, V., Claussen, M., 1998. Simulation of modern and glacial climates with a coupled global model of intermediate complexity. Nature 49, 11–13.

Gierasch, P.J., Goody, R.M., 1968. A study of the thermal and dynamical structure of the Martian lower atmosphere. Planet. Space Sci. 16, 615–646.

Greve, R., Mahajan, R.A., Segschneider, J., Grieger, B., 2004. Evolution of the north-polar cap of Mars: a modelling study. Planet. Space Sci. 52, 775–787.

Haberle, R.M., Pollack, J.B., Barnes, J.R., Zurek, R.W., Leovy, C.B., Murphy, J., Lee, H., Schaeffer, H., 1993. Mars atmospheric dynamics as simulated with the NASA AMES general circulation model. I—the zonal mean circulation. J. Geophys. Res. 98, 3093–3123.

Haberle, R.M., Murphy, J.R., Schaeffer, H., 2003. Orbital change experiments with a Mars general circulation model. Icarus 262, 66–89.

Hoskins, B.J., Simmons, A.J., 1975. A multi-layer spectral model and the semi-implicit method. Q. J. R. Meteorol. Soc. 101, 637–655.

Hourdin, F., Le Van, P., Forget, F., Talagrand, O., 1993. Meteorological variability and the annual surface pressure cycle on Mars. J. Atmos. Sci. 50, 3625–3640.

Jakosky, B.M., 1985. The seasonal cycle of water on Mars. Space Sci. Rev. 41, 131–200.

Joshi, M., Lewis, S., Read, P., Catling, D., 1995. Western boundary currents in the martian atmosphere: numerical simulations and observational evidence. J. Geophys. Res. 100, 5485–5500.

Kieffer, H.H., Zent, A.P., 1992. Quasi-periodic climate change on Mars. In: Kieffer, H.H., Jakosky, B.M., Snyder, C.W., Matthews, M. (Eds.), Mars. University of Arizona Press, Tucson, pp. 767–795.

Kieffer, H.H., Jakosky, B.M., Snyder, C.W., Matthews, M. (Eds.), 1992. Mars. University of Arizona Press, Tucson.

Laskar, J., Levrard, B., Mustard, J.F., 2002. Orbital forcing of the martian polar layered deposits. Nature 419, 375–377.

Laurson, L., Eliasen, E., 1989. On the effects of damping mechanisms in an atmospheric general circulation model. Tellus 41 (A), 385–400.

Leovy, C., Mintz, Y., 1969. Numerical simulation of the atmospheric circulation and climate of Mars. J. Atmos. Sci. 26 (6), 1167–1190.

Michelangeli, D.V., Toon, O.B., Haberle, R.M., Pollack, J.B., 1993. Numerical simulations of the formation and evolution of water ice clouds in the martian atmosphere. Icarus 100, 261–285.

Milankovitch, M., 1930. Mathematische Klimalehre und Astronomische Theorie der Klimaschwankungen. Vol. 1 of Handbuch der Klimatologie in fünf Bänden. Gebrüder, Bornträger, Berlin.

Newman, C.E., Lewis, S.R., Read, P.L., Forget, F., 2002. Modeling the martian dyst cycle. 1: representations of the dust transport processes. 2: multi-annual radiatively active dust transport simulations. J. Geophys. Res. 107 (E12), (1) 5123, (2) 5124 doi:10.1029/2002JE001910.

Rafkin, S.C.R., Maria, M.R.V.S., Michaels, T.L., 2002. Simulation of the atmospheric thermal circulation of a martian volcano using a mesoscale numerical model. Nature 419, 697–699.

Read, P.L., Collins, M., Forget, F., Fournier, R., Hourdin, F., Lewis, S.R., Talagrand, O., Taylor, F.W., Thomas, N.P.J., 1997. A GCM climate database for Mars: for mission planning and for scientific studies. Adv. Space. Res. 19, 1213–1222.

Richardson, M.I., Wilson, R.J., 2002. A topographically forced asymmetry in the martian circulation and climate. Nature 416, 298–301.

Smith, D.E., Zuber, M.T., Solomon, S.C., Phillips, R.J., Head, J.W., Garvin, J.B., Banerdt, W.B., Muhleman, D.O., Pettengill, G.H., Neumann, G.A., Lemoine, F.G., Abshire, J.B., Aharonson, O., Brown, C.D., Hauck, S.A., Ivanov, A.B., McGovern, P.J., Zwally, H.J., Duxbury, T.C., 1999. The global topography of Mars and implications for surface evolution. Science 284, 1495–1503.

Takahashi, Y.O., Fujiwara, H., Fukunishi, H., Odaka, M., Hayashi, Y.-Y., Wanabe, S., 2003. Topographically induced north-south asymmetry of the meridional circulation in the Martian atmosphere. J. Geophys. Res. 108 (E3), 5018 doi:10.1029/2001JE001638.

Wilson, R.J., Hamilton, K., 1996. Comprehensive model simulation of thermal tides in the Martian atmosphere. J. Atmos. Sci. 53, 1290–1326.